Available online at www.sciencedirect.com
SCIENCE DIRECT®
International Journal of Solids and Structures 42 (2005) 4154–4178
INTERNATIONAL JOURNAL OF SOLIDS and STRUCTURES
www.elsevier.com/locate/ijsolstr

Operator-split damage-plasticity applied to groove forming in food can lids

S.H.A. Boers, P.J.G. Schreurs *, M.G.D. Geers

Section of Materials Technology, Department of Mechanical Engineering, Eindhoven University of Technology, P.O. Box 513, 5600 MB Eindhoven, The Netherlands

Received 9 July 2004; received in revised form 1 December 2004

Abstract

This paper presents a numerical–experimental analysis of damage engineering applied to a well-known industrial problem. Many food cans are manually opened by raising a tab on the lid, thus initiating a crack, which is propagated along a circumferential groove. The influence of the groove geometry and depth on the opening force and the resistance against premature opening is investigated for some packaging materials, by making use of dedicated experimental techniques and an operator-split damage-plasticity framework. Attention is focused on a small part of the groove at a location halfway the circular crack-path, 90^0 from the crack initiation point. First, the groove manufacturing is analyzed by pressing a punch into a thin sheet of the material. Grooved specimens are loaded in tension, simulating the internal pressure during sterilization, and in shear, simulating the opening. Experiments have been carried out using a miniaturized tensile/compression stage located in the objective field of an optical microscope. For the computational analysis, an operator-split damage-plasticity model is proposed, where ductile damage is easily operated in conjunction with standard plasticity models. Simulations are done within a geometrically non-linear context, using a hypo-elasto-plastic material model with non-linear hardening and a contact algorithm to simulate the contact bodies in the groove forming process. An arbitrary–Lagrange–Euler (ALE) technique and adaptive remeshing are used to assure mesh quality during the large deformation process. The operator-split procedure used for the solution of the governing equations, allows to make easy use of a non-local damage operator as an extra feature within a commercial FEM package. Experimental results reveal that a reduction up to 20% for the opening force with unchanged pre-opening resistance can be reached with the use of an asymmetric punch for the groove forming. Numerical and experimental results are in good agreement. Simulations show that the industrial process of can lid production can be optimized considerably by controlling damage evolution in the first stage of the process.

Keywords: Canning; Food cans; Groove forming; Softening; Gradient plasticity; Nonlocal damage; ALE; Remeshing

* Corresponding author. Tel.: +31 40 247 2778; fax: +31 40 244 7355.
E-mail address: p.j.g.schreurs@tue.nl (P.J.G. Schreurs).

0020-7683/$ - see front matter
doi:10.1016/j.ijsolstr.2004.12.019

1. Introduction

In recent years, food cans with a completely removable steel lid have become very popular. The customer is able to open the can by hand without using a can opener. In Fig. 1 a modern can lid is presented which in technical terms is called a full aperture easy open end (FAEOE) (Wilson, 1998). A ring shaped tab (1) is riveted onto the lid. In the circumference of the lid, a groove (2) (also called 'score') is made. During opening, the tab is raised and pushed against the countersink (4). The nose of the tab punctures the lid by pushing down one side of the groove, whereas the other side remains attached to the countersink. Next, the tab is pulled in the reverse direction and two cracks propagate along the circular groove. When the two cracks meet, the lid is completely separated from the can.

The opening forces, which must be exerted by the customer, are in many cases still too high. Moreover, the forces vary considerably which may result in the lid suddenly ripping off, leading to dangerous or at least annoying situations. The opening forces can be reduced by making a deeper groove. This, however, compromises the strength of the lid needed to withstand forces during sterilization, transport and storage. In Fig. 2 these two load cases are schematically shown. During sterilization an internal pressure is built up. The lid bulges slightly and the groove is loaded as shown in Fig. 2 on the left. This opening mode is close to and will be referred to as mode-1. During opening of the can, the material around the groove is subjected to

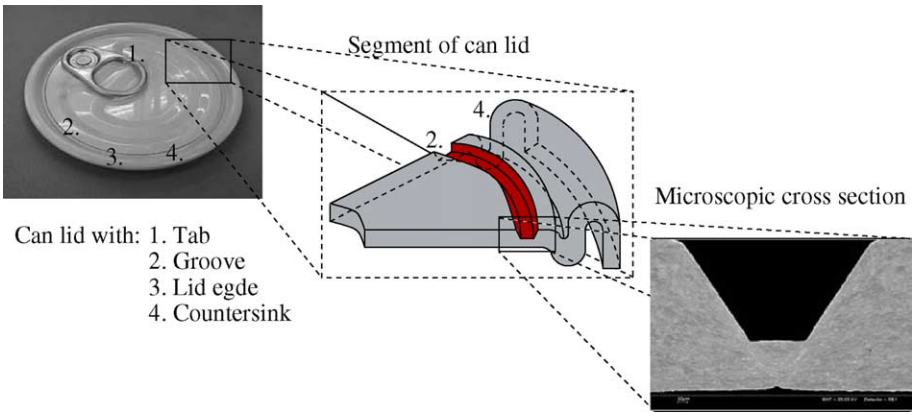

Fig. 1. A can lid is shown (left) and a schematic representation of a segment of the lid with the groove and countersink (middle) and a microscopic cross-section of the grooved region.

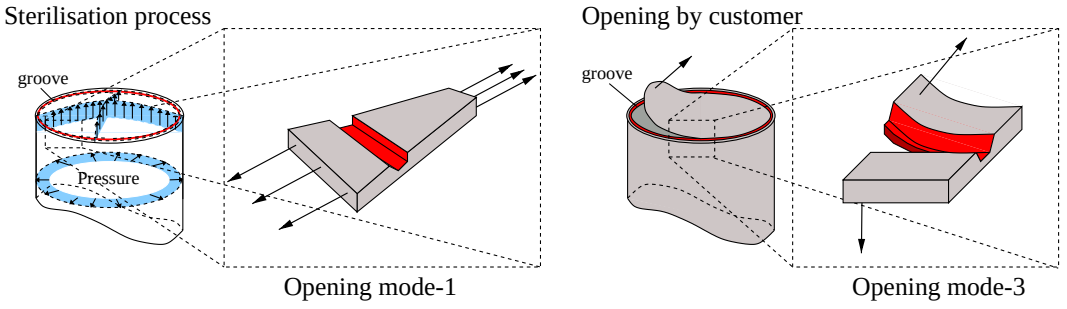

Fig. 2. Loading of the can lid during sterilization (left) and during opening (right).

out-of-plane loading, as shown in Fig. 2 on the right. This opening mechanism is best approached and will be denoted as mode-3.

The commercially used groove depth is based on the can performance during sterilization for which a critical maximum groove depth is already used. In a preliminary study (Boers et al., 2003) it was found that a 25% deeper groove resulted in a 50% decrease in opening force and a 25% decrease in resistance against premature opening. Obviously the damage introduced during groove forming constitutes the limiting factor for the can making industry in the search for improved opening behaviour. The objective of this paper is to reduce the opening mode-3 resistance while maintaining mode-1 strength to prevent premature opening, by means of a numerical-experimental damage engineering analysis. A thorough analysis of damage evolution during groove forming is therefore performed through: (1) dedicated experimental studies of (i) the groove forming process, (ii) mode-1 loading and (iii) mode-3 loading and (2) numerical modelling and simulation of the initiation and propagation of damage in the material during each loading mode. For the latter an operator-split implementation of a damage-plasticity framework is proposed, which allows to use the ductile damage operator in combination with almost any plasticity model available in standard finite element software. Using this damage engineering approach, damage evolution becomes a design parameter rather than an uncontrollable and undesired effect in the process.

Corresponding experiments have been set up and carried out. Grooves are made in thin test samples made from three different packaging materials. Three different punch geometries are used. Materials, experimental setup and test procedures are described in Section 2.1. Groove forming is discussed in Section 2.2. Reaction forces on the punch are analyzed and local deformation fields at the groove region are studied with a microscope. Material damage is directly observed through the presence of voids. The grooved specimens are subsequently subjected to mode-1 and mode-3 loading as described in Sections 2.3 and 2.4. The experiments show that opening forces can be optimized by choosing proper material and a particular punch geometry.

The efficiency of the optimization procedure can be largely improved by numerical simulation of the groove forming process and subsequent analysis of the mode-1 and mode-3 opening behaviour with the finite element method. Whereas several analyses in literature have concentrated on the manufacturing and performance of cans, e.g. (Chu and Biondich, 1994; Courbon, 2003; Gotoh et al., 2003; Hackworth and Henshaw, 2000; Reid et al., 2001; Schünemann et al., 1996; Utsunomiya and Nishimura, 2000; van der Aa et al., 2001; von Diemar, 2000), little work has been done on the opening behaviour for this particular class of cans. To this purpose a plasticity model with a softening yield stress will be used. Various models of this type have been proposed in literature, mostly on the basis of a weakly non-local enrichment (see Aifantis, 1992; Comi and Perego, 1996; de Borst and Mühlhaus, 1992; Liebe and Steinmann, 2001; Mikkelsen, 1999; Pamin, 1994; Ramaswamy and Avaras, 1998; Svedberg and Runesson, 1997; Zervos et al., 2001), and some on the basis of a strongly non-local approach (Bažant and Lin, 1988; Engelen et al., 2003; Geers, 2004; Geers et al., 2001, 2003; Nilsson, 1998; Strömberg and Ristinmaa, 1996). In this paper, an operator-split damage-plasticity model based on the latter category will be used. The elasto-plastic operator applied is based on the Von Mises plasticity model, which is standard in most commercial finite element packages and summarized in Section 3.2. A ductile damage operator is activated in the model since the groove forming experiments clearly showed void nucleation, growth and coalescence resulting in material softening (see also Engelen et al., 2003; Geers, 2004; Geers et al., 2003). The damage evolution is computed from a strongly non-local effective plastic strain, which is obtained as the solution of a second partial differential equation, which has to be solved on the global level, as described in Section 3.3. The equations are solved by making use of an operator-split procedure. The standard equilibrium equation with the plasticity operator is solved using a commercial finite element program, using standard contact algorithms and friction laws. The loading proceeds incrementally and after convergence has been reached in each incremental step, the damage operator is activated. To this purpose, the non-local effective plastic strain is determined by solving a separate boundary value problem. The damage variable is calculated, its degrading influence on the yield stress is incorporated and a new incremental loading step is analyzed.

When the shape of the elements becomes too bad due to large deformations, a remeshing step is included. The complete procedure is described in more detail in Section 3.4.

Analyses of groove forming (Section 4.1) and mode-1 loading (Section 4.2) are performed for the commercially used T67CA material and a trapezoidal groove geometry, from which useful information is obtained by comparing the results with experiments. Practical conclusions are extracted and formulated in Section 5.

Important symbols and notation conventions which are used in this paper are listed in the following table. In mathematical manipulations vectors and tensors are used. Index notation is added for clarity. Also column/matrix notation is indicated.

$\vec{a}$	Vector	a_i	$\underline{a}$
$\mathbf{A}$	Second-order tensor	A_{ij}	$\underline{\underline{A}}$
${}^4\mathbf{A}$	Fourth-order tensor	A_{ijkl}	
$\vec{a}\cdot\mathbf{B}$	Inner product	a_iB_{ij}	$\underline{a}^{\mathrm{T}}\underline{\underline{B}}$
$\mathbf{A}\cdot\mathbf{B}$	Inner product	$A_{ij}B_{jk}$	$\underline{\underline{A}}\,\underline{\underline{B}}$
$\mathbf{A}^d=\mathbf{A}-\frac{1}{3}\mathrm{tr}(\mathbf{A})$	Deviatoric part	$A^d_{ij}=A_{ij}-\frac{1}{3}A_{kk}$	$\underline{\underline{A}}^d=\underline{\underline{A}}-\frac{1}{3}\mathrm{tr}(\underline{\underline{A}})$
$\mathbf{A}{:}\mathbf{B}=\mathrm{tr}(\mathbf{A}\cdot\mathbf{B})$	Double product	$A_{ij}B_{ji}$	$\mathrm{tr}(\underline{\underline{A}}\,\underline{\underline{B}})$

2. Experimental analysis of groove forming and product properties

2.1. Materials, experimental setup and procedure

Three different materials—materials were provided by Corus—are tested. One material, T67CA, is a commercially used packaging steel with an initial yield stress of 507 MPa and a maximum elongation of 16% at fracture during a tensile test. The other materials, T61CA and DR550BA, have yield stresses of 395 MPa and 536 MPa and a maximum elongation at fracture of 18% and 3%, respectively. These materials are all available as sheet metal with a thickness of 210 μm. Their chemical compositions are listed in Table 1. Note that material T67CA has a large percentage Nitrogen (N_{tot}) content of which most is interstitial Nitrogen (N_H).

The complete experimental set-up, in which modular tools for groove forming, mode-1 and mode-3 loading test are used, is illustrated in Fig. 3. The loading stage consists of a firm base on which the motor (1), gearbox (2) and spindle (3) are mounted. Two traverses (4&5) are driven by the spindle and can move from and towards each other with a constant prescribed velocity. The loadcell (6) is positioned at one traverse and the extensiometer (7) at the other. The displacement measurement must be corrected with the elastic deformation of the loadcell to obtain the effective punch displacement relative to the specimen. For the groove forming experiment, an anvil (8) is used, on which the undeformed specimen (9) is clamped (clamps not illustrated). A punch made of hardened steel (10) is placed in a holder (11). The mode-3 experiment consists of a sample holder in combination with a die (12) on which a specimen with two parallel grooves

Table 1
Chemical composition of the selected materials in weight $\%*10^{-3}$, except for N_{tot} and N_H, of which data is given in ppm

Material reference	C	Mn	Al	N_{tot}	N_H	P	S	Si	Cr	Ni	Cu
T67CA	72	349	50	10.9	6.4	15	17	6	21	23	12
T61CA	42	230	58	1.9	0.6	12	16	5	20	24	16
DR550BA	76	353	44	3.3	0.4	14	13	7	21	24	15

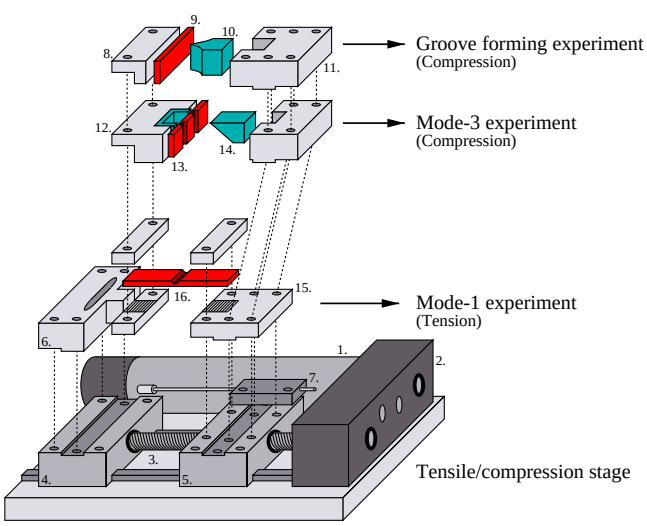

Fig. 3. Schematic representation of the tensile/compression stage on which several tools can be mounted. The tools are presented for the groove forming compression experiment, the mode-3 experiment and the mode-1 experiment.

(13) is placed. A wedge shaped punch (14) pushes the middle part of the specimen into the die-opening. The mode-1 experiment uses the loadcell and a base plate (15) to clamp the mode-1 specimen, which has only one groove (16).

The commercially used punch, provided by Corus, has a trapezoidal shape with an angle of 60° between the side walls and is made of hardened steel. The width of the plateau is 60 μm. It is indicated as TP (trapezoidal punch) and shown in Fig. 4 on the left. In this analysis two other geometries are used which are manufactured through small modifications of the original commercial shape. The first one has one rounded edge, whereas the second shape has two rounded edges. They are referred to as AP (asymmetric punch) and PP (parabolic punch) and are also shown in Fig. 4. It is important to know that the total heights of the punches have not been altered because the width of the punch just beneath the top is an important process parameter. Note that in the industrial groove forming process the radial material flow is suppressed, which will influence the neck formation at the bottom of the samples. Second, the deformation rate is rather high in the industrial practice and may influence the observed damage evolution as well. Nevertheless, the opening behaviour of can lids can be qualitatively well investigated with the proposed set-up, which allows to compare specific punch geometries with different materials.

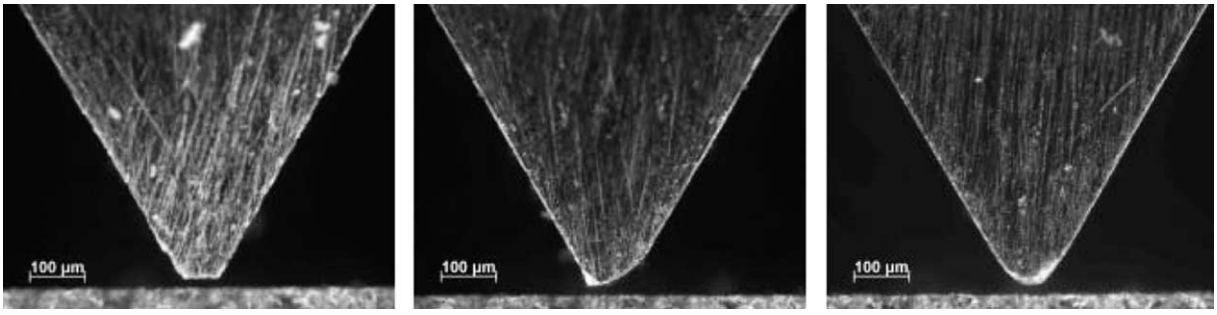

Fig. 4. Punch geometry: trapezoidal (TP), asymmetric (AP) and parabolic (PP).

2.2. Groove forming experiment

In this section the reaction forces on the different punches in combination with different materials are presented for the groove forming experiment. SEM images of resin embedded samples are shown in which some characteristic deformation mechanisms are observed for each punch geometry.

In Fig. 5, the reaction forces are presented per mm sample width vs. the punch displacement in μm (NB: the original thickness is 210 μm). The punch velocity is 1 mm per minute. The deepest grooves, with residual thicknesses of approximately 10 μm can be made with the PP and AP geometries, whereas no grooves deeper than 40 μm can be produced with the commercially used TP geometry. It is noticed that the maximum reaction force with punch geometry TP is reached with material DR550BA.

Resin embedded samples were prepared for all materials. The lateral faces of these samples were observed under the objective of a light microscope and a scanning electron microscope (SEM). For each different groove geometry three different residual thicknesses, i.e. sheet thickness minus groove depth, were considered: 100, 60 and 40 μm. It was observed that samples with the TP geometry contain more material flaws (microvoids) than the PP geometry.

In Fig. 6, groove geometry TP is shown for the three materials and a residual thickness of 60 μm. Clearly, samples made of T61CA material contain less material flaws (microvoids) than the samples made of DR550BA material.

Note that a certain amount of material beneath the flat top surface of the punch is not deformed. This wedge shaped lump of material acts as an extension of the TP punch. This is most obvious from the propagating shear bands, which start along the side walls of the groove and extend towards the bottom. A parabolic shear pattern is formed which is not observed for the PP punch geometry. The samples with an AP geometry present similar shear bands, although they were less extended to the bottom and only present at one side.

In the T67CA material a neck is formed at the bottom of the samples after the punch has moved into the material over a distance of approximately 110 μm, whereas the neck in the DR550BA material is already formed after 90 μm punch displacement. The formation of the neck for the T61CA material occurs after approximately 150 μm punch displacement only. A neck is also formed with the AP geometry for all three

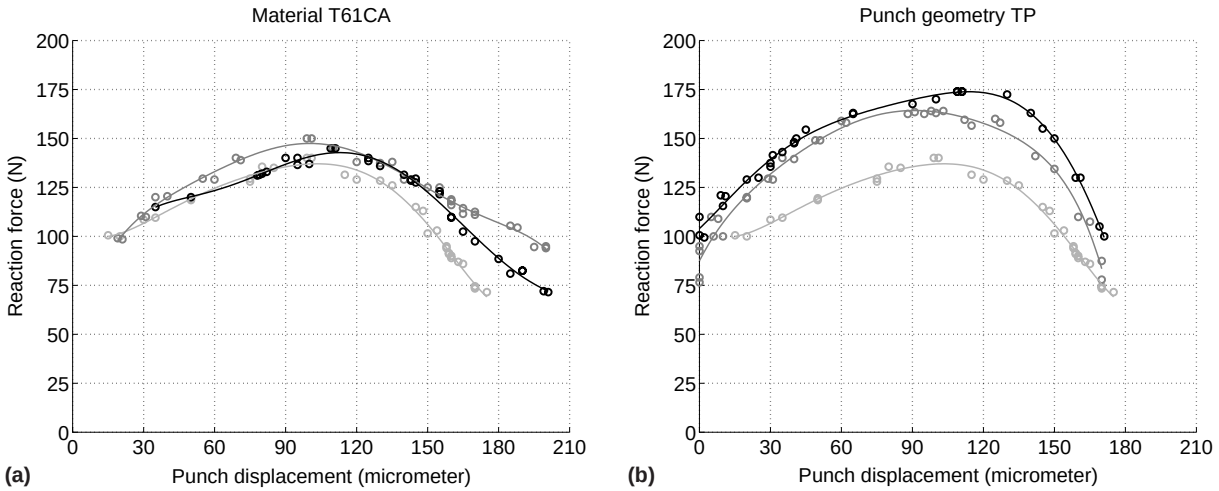

Fig. 5. Reaction force versus punch displacement. Left: T61CA material; PP (black), AP (dark-grey), TP (light-grey). Right: TP; DR550BA (black), T67CA (dark-grey), T61CA (light-grey).

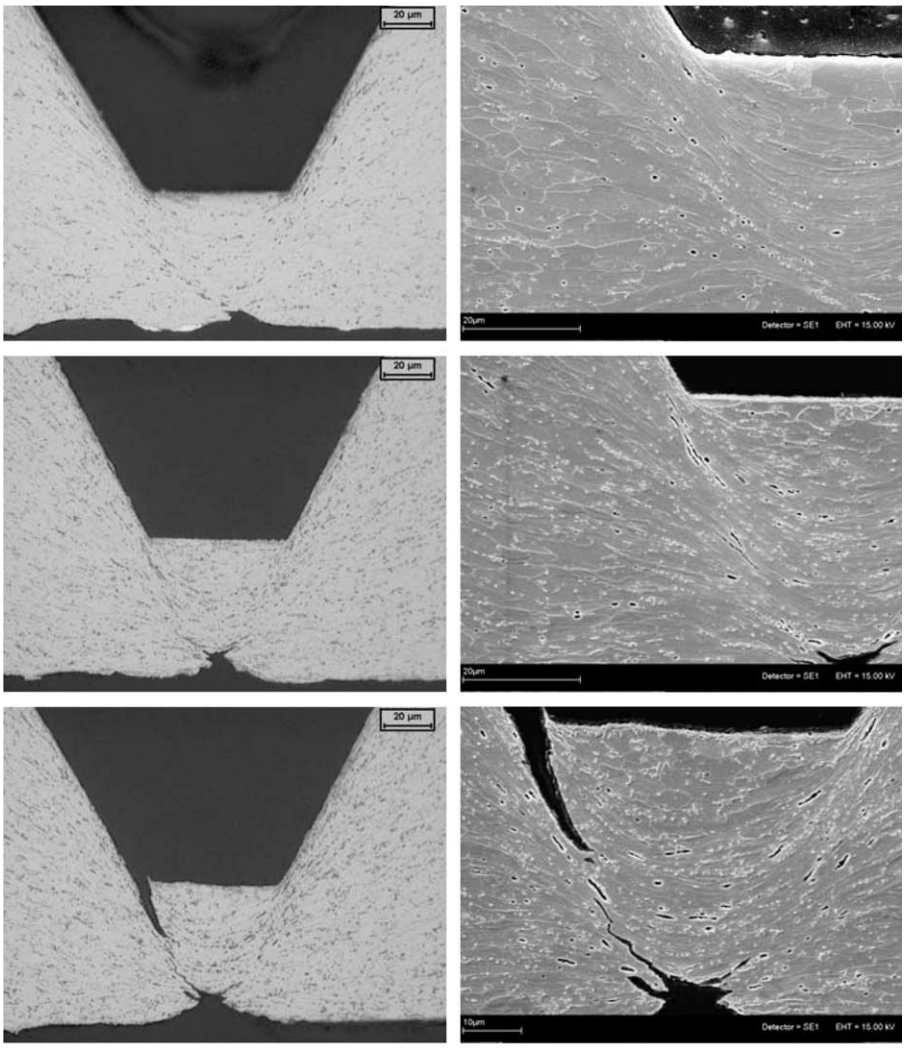

Fig. 6. Top to bottom: material T61CA, T67CA and DR550BA. Left: light microscope images. Right: SEM images. For all samples the groove geometry is TP and the residual thickness 60 μm.

materials, although it is hardly visible. During the groove forming experiment with the PP groove geometry, irrespective of the material used, no necking effect could be observed.

2.3. Mode-1 loading experiment

The mode-1 experiment represents the pre-opening of the lid during the sterilization process. A mode-1 sample with only one groove is clamped and loaded in the plane of the sheet in the direction perpendicular to the groove. In Fig. 7 the mode-1 force is plotted versus the residual thickness of the sample. Each data point corresponds to a separate mode-1 loading experiment on a given sample. The maximum reaction force during each mode-1 experiment is recorded and presented per mm sample width.

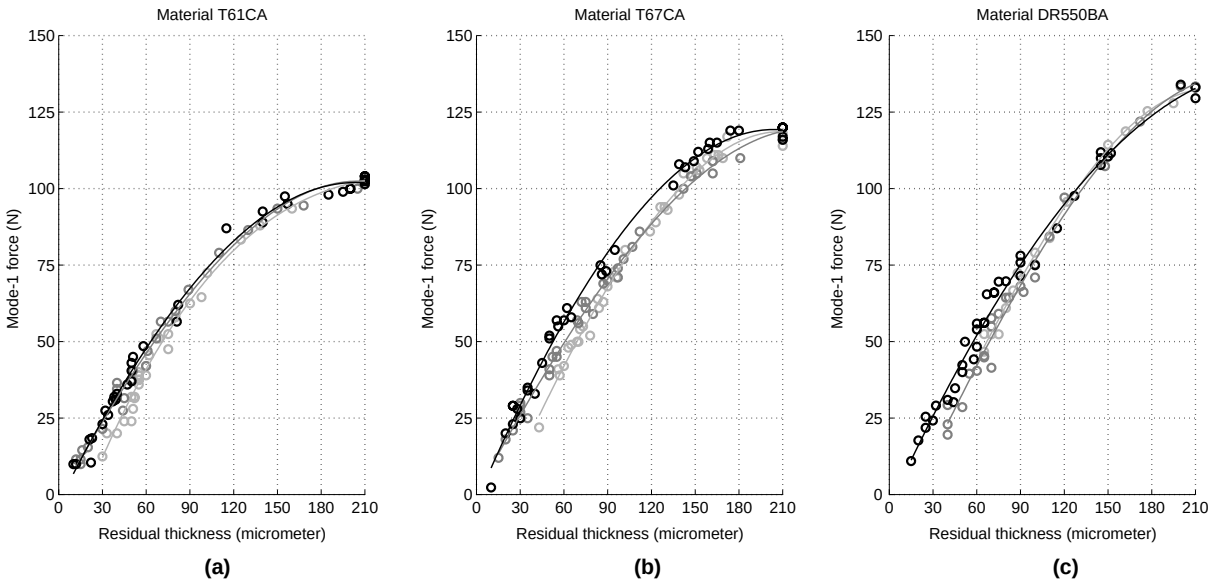

Fig. 7. Mode-1 forces versus punch displacement. Material: T61CA (left), T67CA (middle), DR550BA (right). Punch geometry: PP (black), AP (dark-grey), TP (light-grey).

For the T67CA material and the TP groove geometry, a reduction of the residual thickness from 87 μm to 62 μm (29%) leads to a decrease of the mode-1 force of 23%.

It can be seen clearly, when comparing the three different materials, that the level of mode-1 forces in the 90–210 μm residual thickness region is highest for the DR550BA material and lowest for the T61CA material. In general it can be concluded that the PP groove geometry gives slightly higher mode-1 forces than the other two geometries if an arbitrary residual thickness is considered. For small residual thicknesses, this difference becomes even more significant.

Another remarkable observation is that for the T61CA material, the curves for groove geometry PP and AP are almost identical, whereas the curve for TP diverges from the other two for small residual thicknesses. Similar results can be seen for material DR550BA, although now the curves for groove geometry TP and AP are almost identical and the PP curve diverges from the other two. For material T67CA a certain transition region can be observed in which the AP curve first coincides with the TP curve and then switches to the PP curve.

2.4. Mode-3 loading experiment

The mode-3 experiment approximates the opening by the customer. During the mode-3 experiment, a sample with two parallel grooves is clamped on a die. A wedge shaped punch separates the middle part of the specimen from the outer parts.

Fig. 8 shows the mode-3 forces versus the residual thickness of the samples. These curves are obtained by doing separate mode-3 loading experiments and recording the maximum force for each sample. A variation of residual thickness from 85 μm to 67 μm (21%) reduced the mode-3 forces with 27%.

The trend of the mode-3 force versus the residual thickness is basically the same for all materials and all punch geometries. In the 90–210 μm region of the residual thickness the mode-3 forces decrease considerably with decreasing residual thickness. A remarkable phenomenon for the DR550BA material is noticed where the mode-3 forces reach a maximum at a residual thickness of approximately 180 μm. This effect is

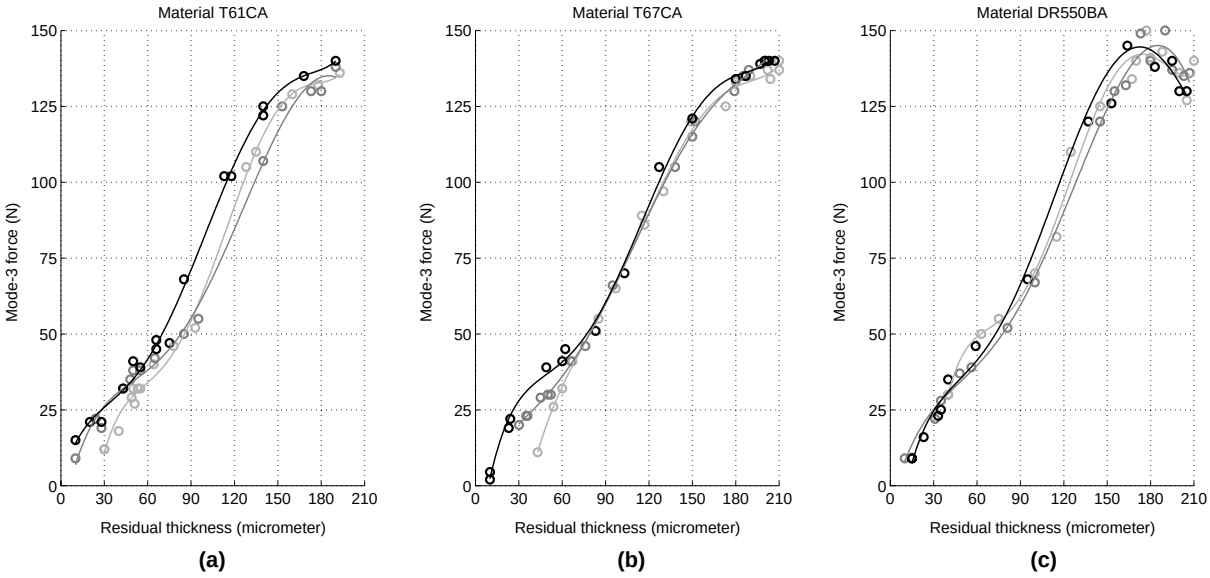

Fig. 8. Mode-3 forces versus punch displacement. Material: T61CA (left), T67CA (middle), DR550BA (right). Punch geometry: PP (black), AP (dark-grey), TP (light-grey).

observed for all the punch geometries in combination with DR550BA material and probably due to plastic bending caused by a slight clearance between the punch and the die opening.

In the 0–90 μm range of the residual thickness a bump deviation can be seen in the mode-3 force curves for all combinations of materials and punch geometries except for material T67CA in combination with the TP punch. For the thinner specimens, the initiation of the mode-3 crack is delayed. This is due to the fact that the material is initially bended and stretched by the anvil resulting in a higher mode-3 force, than would be found for crack propagation only.

2.5. Experimental results resumed

Considerable reduction of mode-3 opening forces can be obtained by making lids with slightly deeper grooves. In the canning industry, can lids of T67CA material and a TP groove geometry are commonly used. The minimum mode-1 force, needed during the sterilization process, is 50 N limiting the residual thickness to a minimum of 70 μm. Any mode-1 sample, irrespective of the material choice and groove geometry, which can withstand a minimum load of 50 N during a mode-1 test should also be able to withstand the load during sterilization. From Fig. 9 on the left, which is an enlargement of Fig. 7 (middle), it can be seen that for samples with groove geometry PP and AP the minimal residual thicknesses must be 52 and 61 μm respectively. The mode-3 forces for these samples can be obtained from Fig. 9 on the right. For all three materials and groove geometries Table 2 lists the minimal residual thicknesses, corresponding mode-3 forces and their reduction with respect to the largest mode-3 force per material, all for a mode-1 force of 50 N.

Characteristic results are:

- The mode-3 forces for the PP geometry are relatively high considering their residual thicknesses. From SEM images it was seen that the PP punch geometry introduces the least visible material flaws into the material during groove forming. Compared to the other two punch geometries, a PP punch can be used

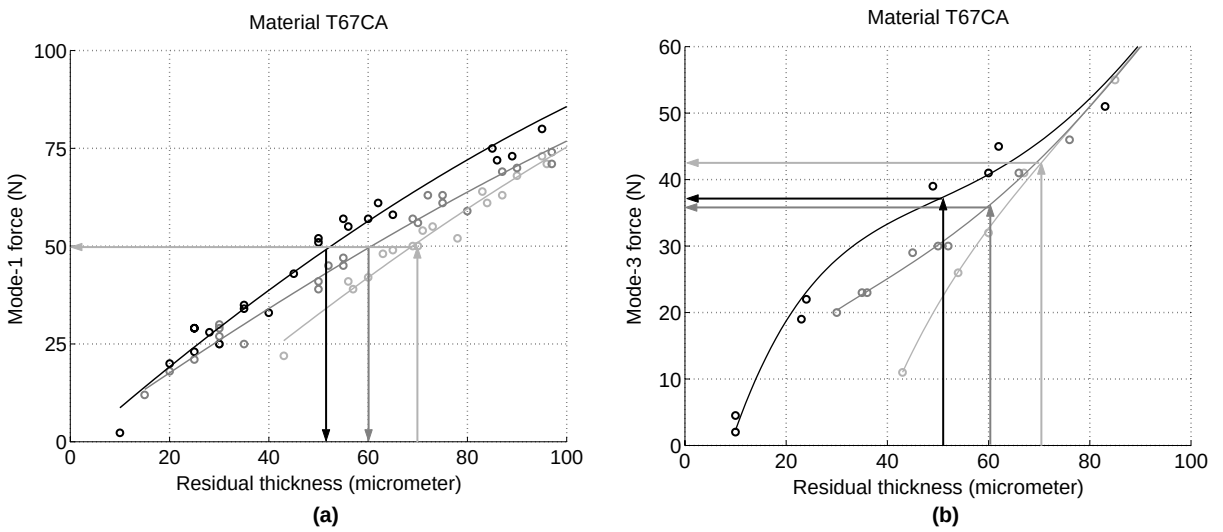

Fig. 9. A close-up of Fig. 7 on the left and Fig. 8 on the right for material T67CA. Punch geometry: PP (black), AP (dark-grey), TP (light-grey).

Table 2
Results of mode-1 and mode-3 experiments summarized

Material	Punch geometry	Residual thickness (micrometer)	Mode-3 force (N)	Reduction mode-3 force in %
T61CA	TP	71	39	11
T61CA	AP	66	41	7
T61CA	PP	63	44	(–)
T67CA	TP	70	44	(–)
T67CA	AP	61	35	20
T67CA	PP	52	37	16
DR550BA	TP	67	52	(–)
DR550BA	AP	68	43	17
DR550BA	PP	57	40	23

to make grooves with a much smaller residual thickness. The necking effect does not occur and as a consequence the mode-1 performance is high which means that samples with a relatively small residual thickness compared to the other two geometries can withstand the minimal 50 N during the mode-1 test. These effects are probably due to the round edges of the punch, which, unfortunately, do not contribute to an effective decrease of the mode-3 force.

- Using the AP geometry effectively reduces the mode-3 forces whilst the strength to prevent pre-opening is retained. Grooved samples showed less material flaws than samples with the TP groove geometry. More flaws were noticed however, compared to samples made with the PP punch. Because of the asymmetry, the necking effect occurs at a later stage during the groove forming test compared to the TP geometry.
- The TP punch geometry introduces the most severe material deformation as apparent from the shear bands and intensity of microcracks around the punch corners (see Fig. 6). A wedge shaped lump of material beneath the flat top of the punch acts as an extension of the punch and moves together with the punch through the material. The sharp edges reduce the mode-3 forces considerably but at the same time the material flaws have a negative effect on the mode-1 performance. For this punch geometry the necking effect is greatest, which is also a disadvantage with respect to mode-1 performance.

- The material that is most suited with respect to mode-1 and mode-3 performance is T67CA, which has a higher deformation capability than DR550BA. The reason for this is that material T67CA contains less material flaws than DR550BA at the same level of deformation. The deformation capability of T67CA is comparable to that of T61CA, however, T67CA has a much higher initial yield stress than T61CA which contributes to a good mode-1 performance for small residual thicknesses.
- Although during the opening of commercially used can lids, the groove opening mode is not completely mode-3, it can be concluded that the opening behaviour can be improved by using the AP groove geometry in combination with the T67CA material: a reduction of 20% for the mode-3 force can be obtained.

Although the experiments already indicate directions for can lid optimization, numerical simulation of groove forming and opening behaviour may lead to an improved predictive insight and an increased efficiency of the procedure.

3. Operator-split ductile damage-plasticity

3.1. Material, numerical models and procedure

The groove forming process and subsequent mode-1 loading experiment are simulated numerically. Finite element analyses are done for the commercially used T67CA material and the TP groove geometry. An elastoplastic Von Mises material model enhanced with ductile damage will be used (see Section 3.2). Material parameters for T67CA are determined experimentally in a standard manner and summarized in Table 3.

The post-yield behaviour of the material cannot be determined in a tensile experiment, because necking will occur at rather small values of the effective plastic strain. To circumvent this problem, a compression test has been carried out according to the setup shown in Fig. 10. A solid cylinder, which can be assumed to

Table 3
Material parameters for T67CA material

Young's modulus	E	207	[GPa]
Poisson's ration	v	0.3	[–]
Initial yield stress	σ_{y0}	507	[MPa]

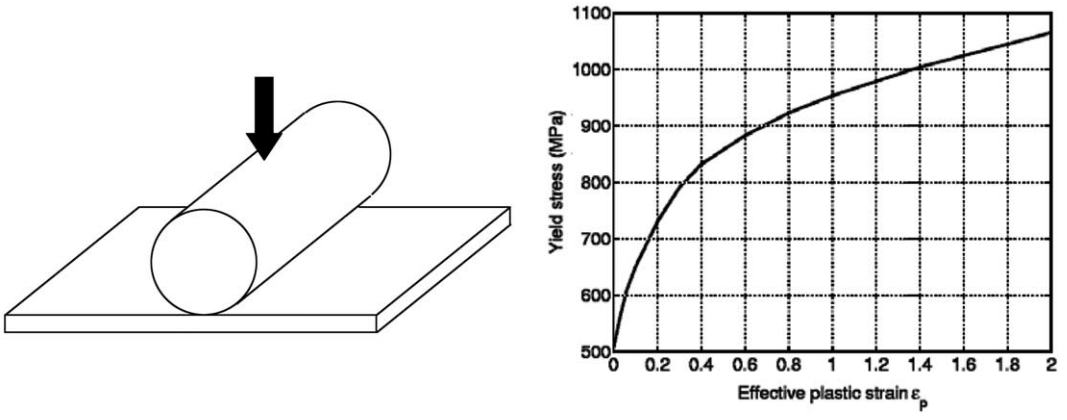

Fig. 10. Yield stress versus effective plastic strain for T67CA material.

be rigid, is pressed into the sheet material with a prescribed force. Due to the non-homogeneous deformation in this test, the hardening curve, relating the yield stress to the effective plastic strain, cannot be determined directly from the experiment. Using an inverse approach, the compression test is simulated numerically with the finite element method. In an iterative procedure the hardening curve was determined by matching experimental data onto the numerical results. The resulting hardening curve is shown in Fig. 10, which is further used in the constitutive description of the material.

To describe the influence of void formation and the resulting material degradation, a plasticity model enhanced with damage has to be used. Among the possible models, elastic-damage with plasticity models may be considered (Abu Al-Rub and Voyiadjis, 2003; Areias et al., 2003; Armero and Oller, 2000a,b; Bruhns et al., 2001; Brünig, 1999; de Borst et al., 1999; de Souza Neto et al., 1994; Li, 1995; Voyiadjis and Kattan, 1990, 1992; Zysset and Curnier, 1996) or typical softening plasticity models (Aifantis, 1992; Bažant and Lin, 1988; Comi and Perego, 1996; de Borst and Mühlhaus, 1992; Engelen et al., 2003; Voyiadjis and Palazotto, 2004; Geers, 2004; Geers et al., 2001, 2003; Liebe and Steinmann, 2001; Mikkelsen, 1999; Nilsson, 1998; Pamin, 1994; Ramaswamy and Avaras, 1998; Strömberg and Ristinmaa, 1996; Svedberg and Runesson, 1997; Zervos et al., 2001). In this contribution a Von Mises plasticity model will be used, enhanced with a ductile damage variable that provides the softening, see also (Jirásek and Rolshoven, 2003) for a comparative analysis. A fully coupled version of this model has been proposed for small and large deformations in Engelen et al. (2003), Geers (2004), Geers et al. (2001, 2003). The strongly non-local character of this softening plasticity model has thereby been clearly emphasized. In this paper, an operator-split version is proposed, in which the damage operator is applied after the plasticity operator in an incremental manner. The evolution of the ductile or plastic damage will be driven by a non-local effective plastic strain (see Section 3.3). Parameters in the damage evolution equations cannot be measured directly but are here determined by comparing experimental and numerical data from the groove forming process, after which they are used in the mode-1 tests.

Stresses and deformation of the material are determined by solving the equilibrium equations together with the constitutive stress–strain relations for the elasto-plastic material behaviour. The non-local effective plastic strain is solved from its evolution equation and determines the value of the damage variable. Due to the history dependent material behaviour and the non-linearity of the equations, an incremental solution procedure is followed and within each increment the equations are solved iteratively. The above equations—equilibrium and non-local strain evolution—can be solved simultaneously for each increment, a so-called fully coupled approach. This calls for a special finite element formulation, where displacements and non-local effective plastic strain are the unknown variables. The equations can also be solved sequentially at the end of each increment, leading to an operator-split version of the model, which will be adopted here. A commercial finite element package is used, where standard features like Von Mises plasticity, contact body modelling and friction models are available to solve the equilibrium equations. Once convergence is reached at the end of each increment and all stresses and deformations are determined, the incremental non-local effective plastic strain averaging equation is solved using a special finite element routine. The damage is then calculated and the yield stress of the material is updated accordingly. When the shape of the elements becomes too bad due to large deformations, a remeshing step is included, which is also done with a separate routine. The complete procedure is described in more detail in Section 3.4.

3.2. Elasto-plastic operator

3.2.1. Kinematics

The transformation of an infinitesimal material volume element from the undeformed configuration t_0 (position vector $\vec{x}_0$) to the deformed—or current—configuration t (position vector $\vec{x}$), is described by the deformation gradient tensor $\mathbf{F} = (\vec{\nabla}_0 \vec{x})^{\mathrm{T}}$, where $\vec{\nabla}_0$ is the gradient operator with respect to the undeformed

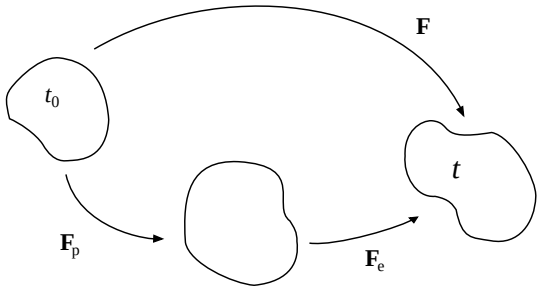

Fig. 11. Elasto-plastic deformation of a material.

state (Lee, 1969). The deformation tensor describes both real deformation and rigid rotation. Various strain tensors can be defined, which describe only the deformation of the material volume.

The deformation rate is described by the velocity gradient tensor $\mathbf{L} = \dot{\mathbf{F}} \cdot \mathbf{F}^{-1} = (\vec{\nabla}\vec{v})^{\mathrm{T}}$, where $\vec{v}$ is the velocity of the material volume and $\vec{\nabla}$ the gradient operator with respect to the deformed state.

The total deformation can be decomposed multiplicatively in a plastic and an elastic deformation: $\mathbf{F} = \mathbf{F}_e \cdot \mathbf{F}_p$ (see Fig. 11). An additive decomposition is used for the velocity gradient tensor : $\mathbf{L} = \mathbf{L}_e + \mathbf{L}_p$. This tensor is composed by its symmetric part, the deformation rate tensor $\mathbf{D}$, and its skew-symmetric part, the spin tensor Ω. Both tensors can be split into an elastic and a plastic part, where it is assumed that the plastic spin tensor equals zero $\Omega_p = \mathbf{O}$

$$\mathbf{D} = \tfrac{1}{2}(\mathbf{L} + \mathbf{L}^{\mathrm{T}}) = \mathbf{D}_e + \mathbf{D}_p; \quad \Omega = \tfrac{1}{2}(\mathbf{L} - \mathbf{L}^{\mathrm{T}}) = \Omega_e \tag{1}$$

3.2.2. Constitutive model

Deformation of the material volume gives rise to stresses and this stress state is described by the symmetric Cauchy stress tensor σ. The relation between the stress state and the deformation is described by constitutive equations, reflecting the response of the material based on experimental observations. In the experiments deformation proceeds slowly, which allows to make the assumption that the material behaviour is not influenced by the deformation rate and that dissipation will not lead to considerable temperature increase of the material. In the following, a fictitious time parameter t will be used to indicate the current state of deformation. The elasto-plastic deformation is described by a Von Mises plasticity model where it is assumed that elastic deformations are infinitesimal, whereas elasto-plastic deformations can be large.

3.2.3. Yield criterion

In elasto-plastic material models, a yield function F is used to evaluate the stress state and to check which deformation mechanism – elastic or elasto-plastic—applies. In the yield criterion an equivalent stress σ_{eq} is compared to the current yield stress σ_y. The yield stress changes due to plastic deformation, which is mathematically described by relating σ_y to a history parameter, here the effective plastic strain ε_p, which is defined by

$$\varepsilon_p = \int_{\tau=0}^{t} \dot{\varepsilon}_p \, \mathrm{d}\tau; \quad \dot{\varepsilon}_p = \sqrt{\tfrac{2}{3}\mathbf{D}_p : \mathbf{D}_p} \tag{2}$$

Only isotropic hardening is considered. The relation between σ_y and ε_p is referred to as the hardening law and must be determined experimentally.

Using the Von Mises equivalent stress, the yield function is written as

$$F(\sigma, \varepsilon_p) = \sigma_{eq}^2 - \sigma_y^2(\varepsilon_p); \quad \sigma_{eq} = \sqrt{\tfrac{3}{2}\sigma^d : \sigma^d} \tag{3}$$

which has to satisfy the well-known Kuhn–Tucker relations

$$\begin{aligned} &\{(F<0)\vee(F=0\wedge\dot{F}<0)\}\rightarrow \text{elastic deformation}\\ &\{(F=0)\wedge(\dot{F}=0)\}\rightarrow \text{elastoplastic deformation}\end{aligned} \tag{4}$$

3.2.4. Elastic deformation

Due to the history and path dependency of the elasto-plastic behaviour, the current stress cannot be related directly to the current strain. The constitutive model is based on a rate formulation where an objective stress rate is related to an objective strain rate. Here we use the objective Jaumann rate of the Cauchy stress tensor, which is defined by

$$\overset{\circ}{\sigma}=\dot{\sigma}-\Omega\cdot\sigma-\sigma\cdot\Omega^{\mathrm{T}} \tag{5}$$

The elastic deformation is described by a linear relation between the Jaumann rate of the Cauchy stress tensor and the deformation rate tensor $\mathbf{D}$ using the fourth-order material tensor ${}^4\mathbf{C}$.

$$\overset{\circ}{\sigma}={}^4\mathbf{C}:\mathbf{D} \tag{6}$$

This relation characterizes a hypo-elastic response, which is not a concern here since elastic deformations are small anyway. The material is assumed to be isotropic in which case the elastic material behaviour is characterized by two material constants, the bulk modulus K and the shear modulus G:

$${}^4\mathbf{C}=\left(K-\tfrac{2}{3}G\right)\mathbf{II}+G({}^4\mathbf{I}+{}^4\mathbf{I}^{\mathrm{RT}}) \tag{7}$$

Here, ${}^4\mathbf{I}=\vec{e}_i\vec{e}_j\delta_{il}\delta_{jk}\vec{e}_k\vec{e}_l$ is the fourth-order unity tensor and ${}^4\mathbf{I}^{\mathrm{RT}}$ its right-hand transposed form.

3.2.5. Elasto-plastic deformation

When the deformation is elasto-plastic, the plastic deformation rate is assumed to be given by the following associative flow rule

$$\mathbf{D}_{\mathrm{p}}=\dot{\lambda}\frac{\partial F(\sigma,\varepsilon_{\mathrm{p}})}{\partial\sigma}=\dot{\lambda}\mathbf{a} \tag{8}$$

where $\dot{\lambda}$ is the plastic multiplier, which has to be determined such that the consistency condition $\dot{F}=0$ is satisfied during plastic deformation. Using $\dot{\varepsilon}_{\mathrm{p}}=\dot{\lambda}\sqrt{\frac{2}{3}\mathbf{a}:\mathbf{a}}$, the consistency condition can be elaborated to

$$F=\tfrac{3}{2}\sigma^d:\sigma^d-\sigma_{\mathrm{y}}^2(\varepsilon_{\mathrm{p}})\rightarrow\dot{F}=3\sigma^d:\dot{\sigma}-2\sigma_{\mathrm{y}}H\dot{\varepsilon}_{\mathrm{p}}=0 \tag{9}$$

Due to the fact that σ^d is symmetric, the material time derivative $\dot{\sigma}$ may be replaced by the Jaumann derivative of the Cauchy stress tensor, yielding

$$3\sigma^d:\overset{\circ}{\sigma}-2\sigma_{\mathrm{y}}H\dot{\varepsilon}_{\mathrm{p}}=0 \tag{10}$$

Using the decomposition $\mathbf{D}=\mathbf{D}_{\mathrm{e}}+\mathbf{D}_{\mathrm{p}}$ the relation between the Jaumann rate of the Cauchy stress tensor and the deformation rate is

$$\overset{\circ}{\sigma}={}^4\mathbf{C}:(\mathbf{D}-\mathbf{D}_{\mathrm{p}})={}^4\mathbf{C}:(\mathbf{D}-\dot{\lambda}\mathbf{a}) \tag{11}$$

which can be substituted in (10) resulting in

$$3\sigma^d:{}^4\mathbf{C}:\mathbf{D}-3\dot{\lambda}\sigma^d:{}^4\mathbf{C}:\mathbf{a}-2\sigma_{\mathrm{y}}H\dot{\lambda}\sqrt{\tfrac{2}{3}\mathbf{a}:\mathbf{a}}=0 \tag{12}$$

The elasto-plastic behaviour is then described by the following set of coupled equations:

$$\left.\begin{aligned} &\overset{\circ}{\sigma} = {}^4\mathbf{C} : (\mathbf{D} - \dot{\lambda}\mathbf{a}) \\ &3\sigma^d : {}^4\mathbf{C} : \mathbf{D} - \dot{\lambda}\left(3\sigma^d : {}^4\mathbf{C} : \mathbf{a} + 2\sigma_y H\sqrt{\tfrac{2}{3}\mathbf{a} : \mathbf{a}}\right) = 0 \end{aligned}\right\} \tag{13}$$

This set of differential equations must be integrated over the deformation history to determine the current value of the stress when the current deformation $\mathbf{F}(t)$ is known. This integration is done incrementally, to which purpose the deformation is discretized in time. A solution of the constitutive and other governing equations is determined at discrete moments in time $\tau = t_i;\ i = \{1, 2, \ldots, n+1\}$, where $\tau = t = t_{n+1}$ is the current time. An interval between two subsequent discrete moments is a time increment and its length Δt may be adapted during the analysis. In the following attention is focused on the current increment $\tau \in [t_n, t_{n+1}]$.

3.2.6. Incremental analysis

The total deformation gradient tensor $\mathbf{F}(t)$ at the current time can be decomposed into the deformation tensor at the start of the current increment, $\mathbf{F}(t_n)$, and the incremental deformation tensor $\mathbf{F}_n(t)$ as shown in Fig. 12. For time τ in the current increment we have

$$\mathbf{F}(\tau) = \mathbf{F}_n(\tau) \cdot \mathbf{F}(t_n) \rightarrow \mathbf{F}_n(\tau) = \mathbf{F}(\tau) \cdot \mathbf{F}^{-1}(t_n) \tag{14}$$

Assuming that all variables at the begin-increment time t_n are known and satisfy all equations, the set of constitutive equations (13) has to be integrated over the current increment $\tau \in [t_n, t_{n+1}]$ when an (approximate) value of the deformation tensor $\mathbf{F}(t_{n+1})$ is known.

The constitutive equations (13) are rewritten in an incremental setting. A stress tensor σ_D is being used, which is invariant for the incremental rigid body rotations. The material time derivative of σ_D is related to the objective Dienes rate $\overset{\diamondsuit}{\sigma}$ of the Cauchy stress tensor

$$\begin{aligned} &\sigma_D = \mathbf{R}_n^T \cdot \sigma \cdot \mathbf{R}_n \rightarrow \dot{\sigma}_D = \mathbf{R}_n^T \cdot \overset{\diamondsuit}{\sigma} \cdot \mathbf{R}_n \\ &\quad \text{with } \overset{\diamondsuit}{\sigma} = \dot{\sigma} - (\dot{\mathbf{R}}_n \cdot \mathbf{R}_n^T) \cdot \sigma - \sigma \cdot (\dot{\mathbf{R}}_n \cdot \mathbf{R}_n^T)^T \end{aligned} \tag{15}$$

Here, $\mathbf{R}_n$ is the incremental rotation tensor determined from the polar decomposition $\mathbf{F}_n = \mathbf{R}_n \cdot \mathbf{U}_n$. It follows that

$$\mathbf{D} = \tfrac{1}{2}\{(\dot{\mathbf{F}} \cdot \mathbf{F}^{-1}) + (\dot{\mathbf{F}} \cdot \mathbf{F}^{-1})^T\} = \tfrac{1}{2}\{\dot{\mathbf{F}}_n \cdot \mathbf{F}_n^{-1} + \mathbf{F}_n^{-T} \cdot \dot{\mathbf{F}}_n^T\} \tag{16}$$

$$= \tfrac{1}{2}\{\dot{\mathbf{R}}_n \cdot \mathbf{R}_n^T + \mathbf{R}_n \cdot \dot{\mathbf{R}}_n^T + \mathbf{R}_n \cdot (\dot{\mathbf{U}}_n \cdot \mathbf{U}_n^{-1} + \mathbf{U}_n^{-1} \cdot \dot{\mathbf{U}}_n) \cdot \mathbf{R}_n^T\} \tag{17}$$

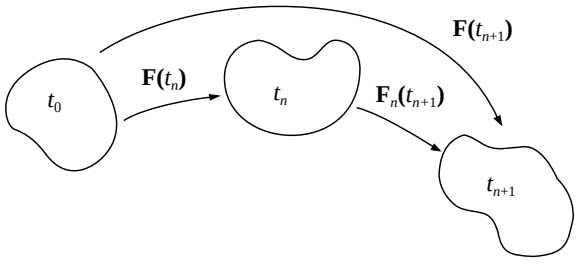

Fig. 12. Incremental deformation: current increment $t_n \rightarrow t_{n+1} = t$ is shown.

It is now assumed that $\mathbf{R}_n$ $(t_n \leqslant \tau < t_{n+1}) = \mathbf{I}$ and that all rigid incremental rotation is concentrated at the end-increment time $\tau = t_{n+1}$. In that case we have for $t_n \leqslant \tau < t_{n+1}$:

$$\begin{aligned} &\sigma_{\mathrm{D}} = \sigma; \quad \overset{\circ}{\sigma} = \overset{\diamondsuit}{\sigma} = \dot{\sigma} \\ &\mathbf{D} = \tfrac{1}{2}(\dot{\mathbf{U}}_n \cdot \mathbf{U}_n^{-1} + \mathbf{U}_n^{-1} \cdot \dot{\mathbf{U}}_n) \end{aligned} \tag{18}$$

When it is also assumed that the incremental principle strain directions are constant during the increment the tensors $\dot{\mathbf{U}}_n$ and $\mathbf{U}_n^{-1}$ are commuting and we have

$$\mathbf{D} = \dot{\mathbf{U}}_n \cdot \mathbf{U}_n^{-1} = \mathbf{U}_n^{-1} \cdot \dot{\mathbf{U}}_n = \sum_{i=1}^{3} \left(\frac{\dot{\lambda}_{ni}}{\lambda_{ni}} \right) \vec{n}_{ni}(t_n) \vec{n}_{ni}(t_n) = \dot{\mathbf{\Lambda}}_n \tag{19}$$

where $\vec{n}_{ni}$ are the incremental principle strain directions and λ_{ni} the associated principle strains. With the invariant tensors the constitutive equations which have to be integrated over the current increment are:

$$\left.\begin{aligned} &\dot{\sigma} = {}^4\mathbf{C} : (\dot{\mathbf{\Lambda}}_n - \dot{\lambda}\mathbf{a}) \\ &3\sigma_{\mathrm{D}}^d : {}^4\mathbf{C} : \dot{\mathbf{\Lambda}}_n - \dot{\lambda}\left(3\sigma_{\mathrm{D}}^d : {}^4\mathbf{C} : \mathbf{a} + 2\sigma_{\mathrm{y}} H \sqrt{\tfrac{2}{3}\mathbf{a} : \mathbf{a}} \right) = 0 \end{aligned}\right\} \tag{20}$$

3.2.7. Integration

An implicit time integration scheme is used to solve the set of equations at the end-increment time $\tau = t = t_{n+1}$. For each time derivative a backward Euler rule is used:

$$\dot{f}(\tau) = \dot{f}(t_{n+1}) = \frac{1}{\Delta t}\{ f(t_{n+1}) - f(t_n) \} \tag{21}$$

Omitting all reference to $\tau = t_{n+1}$ and using $\mathbf{\Lambda}_n(t_n) = \mathbf{O}$, the set of equations becomes

$$\left.\begin{aligned} &\sigma_{\mathrm{D}} = \sigma_{\mathrm{D}}(t_n) + {}^4\mathbf{C} : (\mathbf{\Lambda}_n - \Delta\lambda\mathbf{a}_{\mathrm{D}}) \\ &3\sigma_{\mathrm{D}}^d : {}^4\mathbf{C} : \mathbf{\Lambda}_n - \Delta\lambda\left(3\sigma_{\mathrm{D}}^d : {}^4\mathbf{C} : \mathbf{a} + 2\sigma_{\mathrm{y}} H \sqrt{\tfrac{2}{3}\mathbf{a} : \mathbf{a}} \right) = 0 \end{aligned}\right\} \tag{22}$$

Given the begin-increment state and the incremental logarithmic strain $\mathbf{\Lambda}_n = \mathbf{\Lambda}_n(t_{n+1})$, the stress $\sigma_{\mathrm{D}} = \sigma_{\mathrm{D}}(t_{n+1})$ must be solved from the above system of equations. The solution procedure consists in a standard predictor–corrector or return-mapping algorithm.

3.2.8. Integration procedure

The incremental deformation in a material point may be purely elastic, elastoplastic or partly elastic/elastoplastic. Initially it is assumed that the incremental deformation is purely elastic. The end-increment strain $\mathbf{\Lambda}_n$ is then used to calculate the elastic or trial stress σ_{De}:

$$\sigma_{\mathrm{De}} = \sigma(t_n) + {}^4\mathbf{C}(t_n) : \mathbf{\Lambda}_n \rightarrow \sigma_{\mathrm{e}} = \mathbf{R}_n \cdot \sigma_{De} \cdot \mathbf{R}_n^{\mathrm{T}} \tag{23}$$

where $\mathbf{R}_n$ is calculated from $\mathbf{R}_n = \mathbf{F}_n \cdot \mathbf{U}_n^{-1}$. After computing σ_{e} from (23) the yield criterion is evaluated and when $F(\sigma_{\mathrm{e}}, \varepsilon_{\mathrm{p}}(t_n)) \leqslant 0$ the incremental deformation is assumed to be purely elastic, yielding

$$\sigma(t_{n+1}) = \sigma_{\mathrm{e}}; \quad \varepsilon_{\mathrm{p}}(t_{n+1}) = \varepsilon_{\mathrm{p}}(t_n); \quad \sigma_{\mathrm{y}}(t_{n+1}) = \sigma_{\mathrm{y}}(t_n) \tag{24}$$

When $F(\sigma_{\mathrm{e}}, \varepsilon_{\mathrm{p}}(t_n)) > 0$, the stress $\sigma_{\mathrm{D}}(t_{n+1})$ has to be determined by solving the system of equations (22). Because the equations are non-linear, the solution is determined iteratively.

3.3. Damage operator

In the above constitutive model it was assumed that hardening occurs through which the yield stress increases upon plastic deformation. Upon large tensile or shear deformations, material hardening will decrease upon damage evolution, followed by softening. In the groove forming experiments the reaction forces on the punch decrease after the punch has moved into the material for approximately 110 μm. This decrease is mostly due to the nucleation, growth and coalescence of microvoids. This effect is accounted for by decreasing the yield stress as a function of the effective plastic strain, resulting in material softening (Engelen et al., 2003; Geers, 2004; Geers et al., 2001, 2003). Because the equivalent stress will always be below or equal to the yield stress (i.e. due to the plastic return mapping), the damage has a direct influence on the stress level.

The influence of damage on the yield stress is implemented by a ductile damage parameter ω_p ($0 \leqslant \omega_p \leqslant 1$), which leads to the following formulation of the yield function:

$$F(\sigma, \varepsilon_p, \omega_p) = \sigma_{eq}^2 - [(1-\omega_p)\{\sigma_y(\varepsilon_p)\}]^2 \tag{25}$$

Although void nucleation, growth and coalescence will lead to local anisotropy, the averaged behaviour will be isotropic, which allows the use of a scalar damage variable instead of a damage tensor. As can be seen in Fig. 6, shearing of the material below the die is observed. Because this indicates that mainly the deviatoric deformation is influenced by the material damage, only one damage parameter is used and no volumetric damage component is considered.

The damage parameter ω_p is determined by a material history parameter κ, which is the largest non-local effective plastic strain in a material point. The value for κ must be determined by a non-local parameter otherwise the damage would localize in a narrow band that is governed by the spatial discretizations and the numerical simulation would be meaningless. The equation that is used to determine the non-local effective plastic strain $\bar{\varepsilon}_p$ from the local effective plastic strain ε_p is

$$\bar{\varepsilon}_p - \ell_m^2 \nabla^2 \bar{\varepsilon}_p = \varepsilon_p \tag{26}$$

in which the parameter ℓ_m represents an intrinsic length scale of the material. This parameter is based on the size of e.g. plastic zones during the localization process. On the boundaries the natural boundary condition $\vec{n} \cdot (\vec{\nabla}\bar{\varepsilon}_p) = 0$ is applied.

Although several relations between ω_p and κ have been forwarded (see Engelen et al., 2003; Geers et al., 2003), in this study a simple linear damage evolution law is chosen as a first approximation:

$$\omega_p = \omega_p(\kappa) = 1 - \left(\frac{\kappa_c - \kappa}{\kappa_c - \kappa_i}\right) \tag{27}$$

Damage initiates at a value for κ equal to an initial threshold value κ_i and it reaches a state of total loss of integrity ($\sigma_y = 0$) at a critical value κ_c. The value of ω_p is a linear function of κ, if $\kappa < \kappa_i$ no damage is introduced ($\omega = 0$) and if $\kappa > \kappa_c$ the damage has reached the value of 1.

The set of constitutive equations for the damage enhanced elasto-plastic model are:

$$\left.\begin{aligned} &\sigma_D = \sigma_D(t_n) + {}^4\mathbf{C} : (\boldsymbol{\Lambda}_n - \Delta\lambda\mathbf{a}) \\ &3\sigma_D^d : {}^4\mathbf{C} : \boldsymbol{\Lambda}_n - \Delta\lambda\left(3\sigma_D^d : {}^4\mathbf{C} : \mathbf{a} + 2(1-\omega_p)^2\sigma_y H\sqrt{\tfrac{2}{3}\mathbf{a} : \mathbf{a}}\right) = 0 \end{aligned}\right\} \tag{28}$$

They have to be integrated over the increment to determine the stress state when the deformation is known.

3.4. Operator-split solution strategy

The governing equations which have to be satisfied in every material point at each (discrete) moment of the deformation process, are the equilibrium equation and the differential equation for the non-local effective plastic strain:

$$\left.\begin{aligned} &\vec{\nabla}\cdot\sigma = \vec{0} \\ &\bar{\varepsilon}_{\mathrm{p}} - \ell_{\mathrm{m}}^2\nabla^2\bar{\varepsilon}_{\mathrm{p}} = \varepsilon_{\mathrm{p}} \end{aligned}\right\} \tag{29}$$

The Cauchy stress tensor σ also has to satisfy the constitutive equations (28) which relate the local stress to the local deformation and the damage parameter.

The finite element method, which is used to determine an approximate solution, is based on the weighted residual formulation of the above equations:

$$\left.\begin{aligned} &\int_V \vec{w}\cdot[\vec{\nabla}\cdot\sigma]\mathrm{d}V = 0 \quad \forall \quad \vec{w}(\vec{x}) \\ &\int_V g[\bar{\varepsilon}_{\mathrm{p}} - \ell_{\mathrm{m}}^2\nabla^2\bar{\varepsilon}_{\mathrm{p}} - \varepsilon_{\mathrm{p}}]\mathrm{d}V = 0 \quad \forall \quad g(\vec{x}) \end{aligned}\right\} \tag{30}$$

where $\vec{w}$ and g are weighting functions and V is the material volume in the current, deformed state $t = t_{n+1}$. After partial integration of the first equation and the second term of the second equation, one obtains:

$$\left.\begin{aligned} &\int_V(\vec{\nabla}\vec{w})^{\mathrm{T}} : \sigma\,\mathrm{d}V = \int_S \vec{w}\cdot\vec{p}\,\mathrm{d}S = f_{eu} \quad \forall \quad \vec{w}(\vec{x}) \\ &\int_V g\bar{\varepsilon}_{\mathrm{p}}\,\mathrm{d}V + \int_V(\vec{\nabla}g)\cdot(\vec{\nabla}\bar{\varepsilon}_{\mathrm{p}})\ell_{\mathrm{m}}^2\,\mathrm{d}V = \int_V g\varepsilon_{\mathrm{p}}\,\mathrm{d}V = f_{e\varepsilon} \quad \forall \quad g(\vec{x}) \end{aligned}\right\} \tag{31}$$

where Gauss' theorem is used in both equations and where the stress vector $\vec{p} = \sigma\cdot\vec{n}$ and the boundary condition $\vec{n}\cdot(\vec{\nabla}\bar{\varepsilon}_{\mathrm{p}}) = 0$ have been substituted. In here, $\vec{n}$ is the external unit normal vector in a point of the boundary S.

A fully coupled solution for plasticity with ductile damage has been presented in Engelen et al. (2003), Geers (2004), Geers et al. (2003) for a different plasticity model. Here a different approach will be followed where the equations are solved using an operator split approach. The equilibrium equation (31a) is solved first for each increment for known begin-increment values $\omega_{\mathrm{p}}(t_n)$, $\kappa(t_n)$, $\bar{\varepsilon}_{\mathrm{p}}(t_n)$ and $\varepsilon_{\mathrm{p}}(t_n)$.

Due to the large deformations the integral over the unknown domain V has to be transformed to an integral over the known begin-increment configuration (updated Lagrange procedure). In each increment the integral equation must be solved iteratively. All unknown end-increment variables are written as the sum of a known approximate value ()* and its iterative change $\delta(\,)$. After substitution in the integral equations, these are linearized w.r.t. the iterative variables, leading to the iterative integral equation

$$\int_{V^*}[\mathbf{L}_w^* : \sigma^*\mathbf{I} : \mathbf{L}_u^{*\mathrm{T}} - \mathbf{L}_w^* : (\sigma^{*T}\cdot\mathbf{L}_u^{*\mathrm{T}})^{\mathrm{T}} + \mathbf{L}_w^* : \delta\sigma]\mathrm{d}V^* = r_{eu}^* \tag{32}$$

with $\mathbf{L}_w^* = (\vec{\nabla}^*\vec{w})^{\mathrm{T}}$ and $\mathbf{L}_u^* = (\vec{\nabla}^*\delta\vec{u})^{\mathrm{T}}$. The right-hand side of the equation is the residual. In each iteration step the stress σ has to be updated according to the constitutive equation system described before. Also the iterative change $\delta\sigma$ has to be related to the iterative displacement $\delta\vec{u}$ using the consistent material stiffness tensor ${}^4\mathbf{M}^*$ which can be derived from the incremental constitutive equations (28):

$$\delta\sigma = {}^4\mathbf{M}^* : \mathbf{L}_u^* \tag{33}$$

The unknown iterative displacement $\delta\vec{u}$ is solved from the iterative integral equations using the finite element method. After reaching convergence of the iterative procedure, the end-increment deformation $\mathbf{F}(t_{n+1})$ and stress state $\sigma(t_{n+1})$ are known.

In a second calculation the non-local strain $\bar{\varepsilon}_{\mathrm{p}}$ is solved from (31b). Transformation of the integral is not needed because $V = V(t_{n+1})$ is known. The equation is linear and solved directly for the non-local strain $\bar{\varepsilon}_{\mathrm{p}}$

using a finite element approximation. Material parameters are then updated according to the relations from Section 3.3.

3.4.1. Finite element method

Four-node elements are used for spatial discretization with linear interpolation of the iterative displacement and the non-local effective plastic strain. Following the Galerkin method, the weighting functions are interpolated analogously. After writing vectors and tensors w.r.t. a suitable vector basis, the next (incrementally) uncoupled set of algebraic (iterative) equations are obtained:

$$\underline{\underline{K}}^{*}_{u}\delta\underset{\sim}{u} = \underset{\sim}{r}^{*}_{eu} \tag{34}$$

$$\underline{\underline{K}}_{\varepsilon}\underset{\sim}{\bar{\varepsilon}}_{p} = \underset{\sim}{f}_{e\varepsilon} \tag{35}$$

Solving Eq. (31) in an operator-split manner offers the possibility to use commercial plasticity codes in a straightforward manner. The equilibrium equation with Von Mises plasticity as described in the former section is solved first, i.e. using the MSC.MARC finite element package, which features large strain contact analyses with friction.

At the end of each increment, after reaching convergence, the non-local effective plastic strain is solved from Eq. (35) using a separate FE routine, which can be either commercial or user-made. The value of the yield stress σ_y is then updated by calculating the current value of the ductile damage. The system is thus solved by solving the following equations sequentially for each increment:

$$\begin{aligned} &\underline{\underline{K}}^{*}_{u}\delta\underset{\sim}{u} = \underset{\sim}{r}^{*}_{eu} : \text{MSC.MARC} \\ &\underline{\underline{K}}_{\varepsilon}\underset{\sim}{\bar{\varepsilon}}_{p} = \underset{\sim}{f}_{e\varepsilon} : \text{Separate FE routine} \end{aligned} \tag{36}$$

The main advantage of the operator-split approach proposed is the fact that the damage operator can be used in a straightforward manner in combination with any plasticity operator as available in most commercial FE packages. The disadvantage with respect to a fully coupled procedure is the fact that the incremental loading steps must be rather small in order to reduce the error introduced by splitting both operators. Note that these small steps are often required for the contact algorithm as well.

3.4.2. Remeshing

Due to the large deformations, the finite element mesh needs regular adaptation to guarantee good element shape quality. Updating of the mesh is also done in a user code according to the following procedure.

First, following the arbitrary–Lagrange–Euler (ALE) (Schreurs et al., 1986) method, translated more favorable positioned nodes are calculated, resulting in a new mesh with an improved quality. The topology of the mesh and the nodes on the contour are fixed during this procedure. Transport of state variables is done with the discontinuous Galerkin (DG) method as described in van der Aa et al. (2001). From Brokken (1999) it is known that this method is relatively accurate for small nodal displacements but becomes more diffusive for larger nodal displacements. In Brokken (1999), some numerical tests have been performed in which the accuracy of the transport algorithm is assessed when the size of the elements and the number of transport steps are varied. The spatial scales and deformation gradients in the blanking analysis from Brokken (1999) are comparable to the ones occurring in the groove forming analysis in this study. It appeared that the DG method is capable of solving the transport equations with sufficient accuracy for the mesh of the groove forming experiment if the element size is comparable to the element size in the numerical blanking analysis from Brokken (1999).

The ALE method can improve the mesh quality to a certain extent but is unable to maintain the preferred mesh quality towards the end of the groove forming analysis. Therefore a supplementary adaptive

remeshing procedure is required after a number of increments. The adaptive remeshing procedure, which is described in Brokken (1999), tries to obtain an ideal mesh with respect to the accuracy of the solution, while keeping the mesh as coarse as possible to minimize computational costs. Elements can be added or removed and moreover, the size and density of the elements is changed as a function of the gradient of the state variable field. A reconstruction of the state variable field is done with the superconvergent patch recovery (SPR) technique. A continuous state variable field on the nodes of the non-adapted mesh is determined from a discontinuous state variable field based on the element integration points, after which a state variable field is computed for the new mesh.

Of course some errors are introduced when the state variable field from the new (discrete) mesh is compared to the continuous state variable field which was obtained by the SPR technique. If the error, for a certain region, has not exceeded a specified threshold value, the trial solution and trial mesh will be adopted as the new mesh. If this error exceeds the threshold value, a new mesh is defined which will capture the continuous state variable field better than the old trial mesh. This can happen if the old trial mesh does not contain elements that are small enough in order to capture the gradients in the continuous state variable field in a sufficiently accurate manner. New mesh topology and integration point data are transferred back to the commercial finite element code and a new increment is started. After certain increments in the groove forming analysis, data are saved for later use as a starting point for mode-1 loading simulations.

4. Numerical analysis of groove forming and product properties

4.1. Groove forming simulation

In the simulation of the groove forming experiment contact procedures are needed to simulate the punch and anvil. Also a sample holder is simulated because the sides of the samples in the experiment are constrained in one direction. These tools are all modelled as rigid bodies. Dry friction is modelled with a friction coefficient of 0.1, which is a generally applied value for metals.

In Fig. 13, ω_p is presented for a simulation of the groove forming test in which $\kappa_i = 2$, $\kappa_c = 10$ and $l_m = 10^{-3}$ mm. The damage is concentrated in a narrow band which starts at the side of the groove and extends towards the bottom of the sample. In the enlarged pictures it is seen that the predicted damage zone

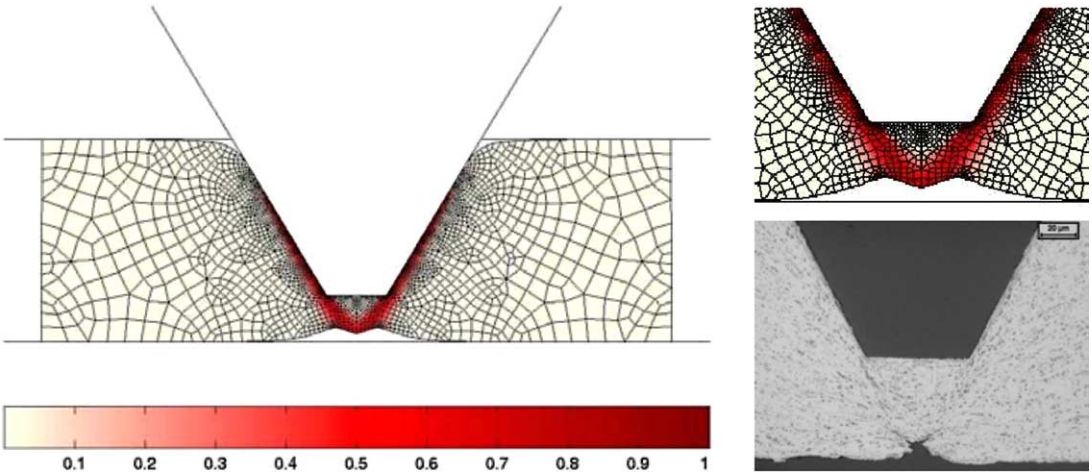

Fig. 13. Punch displacement 168 μm; the value for ω_p is shown.

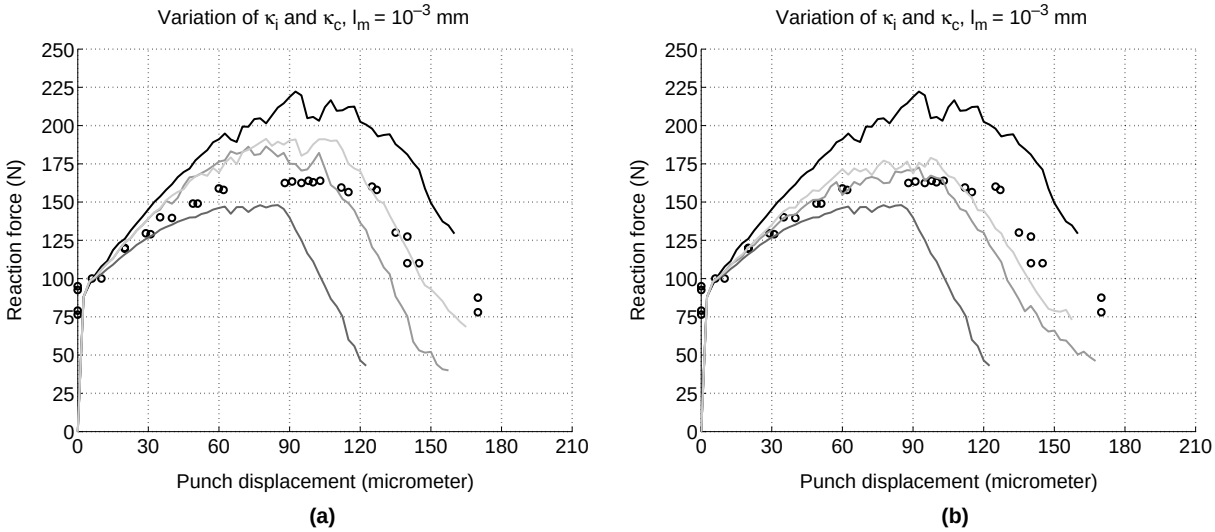

Fig. 14. Results of groove forming experiment (black dots) and simulation (lines) for $l_m = 10^{-3}$ mm. The black line represents results with no damage incorporated. left: $\{\kappa_i, \kappa_c\} = \{0,3\}$ (d-grey), $\{1,4\}$ (grey), $\{2,5\}$ (l-grey). right: $\{\kappa_i, \kappa_c\} = \{0,3\}$ (d-grey), $\{0,6\}$ (grey), $\{0,10\}$ (l-grey).

coincides well with the zone of voiding and shearing, as observed with the light microscope during groove forming. The damage parameters κ_i and κ_c and the internal length parameter ℓ_m cannot be measured directly. They are determined by comparison of the measured and calculated groove forming punch forces. First, several combinations of κ_i and κ_c are chosen at a fixed value for the internal length $\ell_m = 10^{-3}$ mm. From Fig. 14 (left) it can be concluded that the initial value for the maximum effective plastic strain κ_i must be chosen to be zero (0), because otherwise the calculated forces will be too high, especially for the smaller punch displacements (<120 μm). Variation of κ_c at $\kappa_i = 0$ indicates that the sets $\{\kappa_i, \kappa_c\} = \{0,6\}$ and $\{\kappa_i, \kappa_c\} = \{0,10\}$ give the best results for $\ell_m = 10^{-3}$ mm as can be seen in Fig. 14 (right). Simulations were also done with a larger internal length parameter value: $\ell_m = 10^{-2}$ mm. However, an increase of ℓ_m represents a more ductile material behaviour with a wider damage band, resulting in punch forces being too high for all combinations $\{\kappa_i, \kappa_c\}$. In the simulation of the mode-1 loading experiment $\{\kappa_i, \kappa_c\} = \{0,6\}$ and $\{\kappa_i, \kappa_c\} = \{0,10\}$ are used with $\ell_m = 10^{-3}$ mm.

4.2. Mode-1 loading simulation

At several fixed time intervals during the groove forming experiment, a set of data is saved. These data sets are used to start the mode-1 loading analyses for samples with different residual thicknesses. For mode-1 loading the displacement of the right side of the model is prescribed incrementally and the reaction force is recorded.

In Fig. 15 experimental and numerical results are shown for the mode-1 forces. It appears that for $\ell_m = 10^{-3}$ mm both combinations $\{\kappa_i, \kappa_c\} = \{0,6\}$ and $\{\kappa_i, \kappa_c\} = \{0,10\}$ lead to results which compare well to the experimental data.

It is obvious that the calculated mode-1 forces depend on the damage which is introduced during the earlier groove forming simulation. Although mode-3 opening is not analyzed because this would have required a much more complicated numerical model, it can be concluded that the concept of damage engineering is a valuable approach for the design of industrial products.

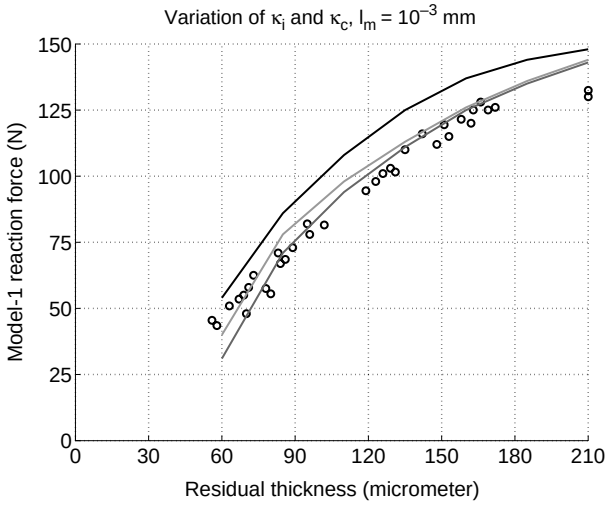

Fig. 15. Results of mode-1 experiments (dots) and simulations (lines). $l_m = 10^{-3}$ mm; $\{\kappa_i, \kappa_c\}$ = no damage (black), $\{0,6\}$ (dark-grey), $\{0,10\}$ (grey).

4.3. Numerical results resumed

Comparing the results from experiments and numerical simulations leads to the following conclusions:

- The numerically calculated forces for groove forming and mode-1 loading compare well to the experimental values.
- The damage fields compare well to the experimental observations.
- In the absence of detailed micromechanical information, a linear damage evolution has been assumed as a first-order approximation. Nevertheless, qualitatively meaningful results have been obtained. Evidently, a more elaborate fitting procedure can be performed to obtain more precise values for the damage evolution parameters κ_i, κ_c and l_m. Also more complicated relations between ω_p and κ can be explored.
- Controlled damage initiation and evolution in some stage of the production process can be exploited in the later production steps.

5. Conclusions

In this paper, a numerical–experimental damage engineering analysis has been performed that provides new insights into the relation between the groove forming process and the mode-1 and mode-3 opening forces of grooved food can lids.

The experimental analysis has shown that the dependence of opening forces on residual groove thickness differs for various punch geometries and specimen materials. The best opening behaviour, i.e. lowest mode-3 force at good mode-1 resistance, could be realized with the commercially used T67CA material with an asymmetric punch (AP) for groove forming.

Although three punch geometries and three materials were investigated experimentally, the efficiency of the optimization of can lid design and groove forming process can be supported by numerical simulations.

For this purpose an operator-split damage-plasticity model has been proposed, which has been implemented in a geometrically non-linear framework with contact. A non-local ductile damage operator is computed at the end of each converged plasticity increment, leading to an incremental update of the yield stress in all material points. The model is evaluated for one punch geometry (TP) and one material (T67CA). Experimental and numerical deformation and damage fields as well as forces have been compared, presenting a good agreement for the parameter set used. Friction is shown to increase the level of the reaction force in the groove forming simulations considerably.

The operator-split solution procedure allows to implement ductile damage in a straightforward manner within a commercial finite element code, where various plasticity models can be easily combined with the damage operator. The coupling of damage to a commercial finite element package enables the use of a large class of constitutive models, contact algorithms, pre- and post-processing features, etc. Material damage, generated in a first stage of the production process (groove forming) can be predicted together with its influence on the subsequent deformation process. This possibility opens new routes towards sophisticated damage engineering strategies, where damage is allowed to develop in a controlled way and where the efficiency of the fabrication process and the final product can be enhanced.

Acknowledgment

The research presented in this paper was supported by Corus RD&T, IJmuiden, The Netherlands, who provided materials and punches. Special thanks goes to Erik van der Aa, Maarten de Haas and Ron Teunissen for their contributions. Part of the research was carried out with the support of the Netherlands Institute for Metals Research (www.nimr.nl), which is gratefully acknowledged.

References

Abu Al-Rub, R.K., Voyiadjis, G.Z., 2003. On the coupling of anisotropic damage and plasticity models for ductile materials. International Journal of Solids and Structures 40 (11), 2611–2643.

Aifantis, E.C., 1992. On the role of gradients in the localization of deformation and fracture. International Journal of Engineering Science 30, 1279–1299.

Areias, P.M.A., César de Sá, J.M.A., Conceição António, C.A., 2003. A gradient model for finite strain elastoplasticity coupled with damage. Finite Elements in Analysis and Design 39 (13), 1191–1235.

Armero, F., Oller, S., 2000a. A general framework for continuum damage models. I. Infinitesimal plastic damage models in stress space. International Journal of Solids and Structures 37 (48–50), 7409–7436.

Armero, F., Oller, S., 2000b. A general framework for continuum damage models. II. Integration algorithms, with applications to the numerical simulation of porous metals. International Journal of Solids and Structures 37 (48–50), 7437–7464.

Bažant, Z.P., Lin, F.-B., 1988. Nonlocal yield limit degradation. International Journal for Numerical Methods in Engineering 26, 1805–1823.

Boers, S.H.A., Schreurs, P.J.G., Geers, M.G.D., 2003. Computational damage engineering for the groove forming in food cans. In: Proceedings of the 7th International Conference on Computing Plasticity (COMPLAS VII). Barcelona, Spain, pp. on CD-rom.

Brokken, D., 1999. Numerical modelling of ductile fracture in blanking. Ph.D. thesis, Eindhoven University of Technology, Eindhoven, The Netherlands.

Bruhns, O.T., Xiao, H., Meyers, A., 2001. A self-consistent Eulerian rate type model for finite deformation elastoplasticity with isotropic damage. International Journal of Solids and Structures 38 (4), 657–683.

Brünig, M., 1999. A framework for large strain elastic–plastic damage mechanics based on metric transformations. International Journal of Engineering Science 39 (9), 1033–1056.

Chu, E.W., Biondich, S.C., 1994. Understanding of coining beverage can ends. Journal of Materials Processings and Manufacturing Science 2 (3), 285–303.

Comi, C., Perego, U., 1996. A generalized variable formulation for gradient-dependent softening plasticity. International Journal for Numerical Methods in Engineering 39, 3731–3755.

Courbon, J., 2003. Damage evolution in a compressive forming process: ironing of beverage cans. Scripta Materialia 48 (11), 1519–1524.
de Borst, R., Mühlhaus, H., 1992. Gradient-dependent plasticity: formulation and algorithmic aspects. International Journal for Numerical Methods in Engineering 35, 521–539.
de Borst, R., Pamin, J., Geers, M.G.D., 1999. On coupled gradient-dependent plasticity and damage theories with a view to localization analysis. European Journal of Mechanics-A/Solids 18 (6), 939–962.
de Souza Neto, E.A., Perić, D., Owen, D.R.J., 1994. Model for elastoplastic damage at finite strains: algorithmic issues and applications. Engineering Computations 11 (3), 257–281.
Engelen, R.A.B., Geers, M.G.D., Baaijens, F.P.T., 2003. Nonlocal implicit gradient-enhanced softening plasticity. International Journal of Plasticity 19 (4), 403–433.
Geers, M.G.D., 2004. Finite strain logarithmic hyperelasto-plasticity with softening: a strongly nonlocal implicit gradient framework. Computer Methods in Applied Mechanics and Engineering 193 (30–32), 3377–3401.
Geers, M.G.D., Engelen, R.A.B., Ubachs, R.L.J.M., 2001. On the numerical modelling of ductile damage with an implicit gradient-enhanced formulation. Revue européenne des éléments finis 10 (2–4), 173–193.
Geers, M.G.D., Ubachs, R.L.J.M., Engelen, R.A.B., 2003. Strongly nonlocal gradient-enhanced finite strain elastoplasticity. International Journal for Numerical Methods in Engineering 56 (14), 2039–2068.
Gotoh, M., Kim, Y., Yamashita, M., 2003. A fundamental study of can forming by the stretch-drawing process. Journal of Materials Processing Technology 138 (1–3), 545–550.
Hackworth, M.R., Henshaw, J.M., 2000. A pressure vessel fracture mechanics study of the aluminum beverage can. Engineering Fracture Mechanics 65 (5), 525–539.
Jirásek, M., Rolshoven, S., 2003. Comparison of integral-type nonlocal plasticity models for strain-softening materials. International Journal of Engineering Science 41 (13–14), 1553–1602.
Lee, E.H., 1969. Elastic–plastic deformations at finite strains. Journal of Applied Mechanics, 1–6.
Li, X., 1995. Large strain constitutive modelling and computation for isotropic, creep elastoplastic damage solids,. International Journal for Numerical Methods in Engineering 38 (5), 841–860.
Liebe, T., Steinmann, P., 2001. Theory and numerics of a thermodynamically consistent framework for geometrically linear gradient plasticity. International Journal for Numerical Methods in Engineering 51 (12), 1437–1468.
Mikkelsen, L.P., 1999. Necking in rectangular tensile bars approximated by a 2-D gradient dependent plasticity model. European Journal of Mechanics A/Solids 18, 805–818.
Nilsson, C., 1998. On nonlocal rate-independent plasticity. International Journal of Plasticity 14 (6), 551–575.
Pamin, J., 1994. Gradient-dependent plasticity in numerical simulation of localization phenomena. Ph.D. thesis, Delft University of Technology, Delft.
Ramaswamy, S., Avaras, N., 1998. Finite element implementation of gradient plasticity models. Part ii: Gradient-dependent evolution equations. Computer Methods in Applied Mechanics and Engineering 163, 33–53.
Reid, J.D., Bielenberg, R.W., Coon, B.A., 2001. Indenting, buckling and piercing of aluminum beverage cans. Finite Elements in Analysis and Design 37 (2), 131–144.
Schreurs, P.J.G., Veldpaus, F.E., Brekelmans, W.A.M., 1986. Simulation of forming processes, using the arbitrary Eulerian–Lagrangian formulation. Computer Methods in Applied Mechanics and Engineering 58, 19–36.
Schünemann, M., Ahmetoglu, M.A., Al, T., 1996. Prediction of process conditions in drawing and ironing of C. Journal of Materials Processing Technology 59 (1–2), 1–9.
Strömberg, L., Ristinmaa, M., 1996. Fe-formulation of a nonlocal plasticity theory. Computer Methods in Applied Mechanics and Engineering 136 (1–2), 127–144.
Svedberg, T., Runesson, K., 1997. A thermodynamically consistent theory of gradient-regularized plasticity coupled to damage. International Journal of Plasticity 13 (6–7), 669–696.
Utsunomiya, H., Nishimura, H., 2000. Effect of base profile of a di beverage can and material properties on the dome reversal pressure. Journal of Materials Processing Technology 97 (1–3), 54–60.
van der Aa, M.A.H., Schreurs, P.J.G., Baaijens, F.P.T., 2001. Modelling of the wall ironing process of polymer coated sheet metal. Mechanics of Materials 33, 555–572.
von Diemar, O., 2000. Packaging with steel—prospects for the beverage can. Stahl und Eisen 120 (5), 55–59.
Voyiadjis, G.Z., Kattan, P.I., 1990. Coupled theory of damage mechanics and finite strain elasto-plasticity. II. Damage and finite strain plasticity. International Journal of Engineering Science 28 (6), 505–524.
Voyiadjis, G.Z., Kattan, P.I., 1992. Plasticity-damage theory for large deformation of solids. I. Theoretical formulation. International Journal of Engineering Science 45 (3), S95–S109.
Voyiadjis, G.Z., Palazotto, R.K.A., 2004. Thermodynamic framework for coupling of non-local viscoplasticity and non-local anisotropic viscodamage for dynamic localization problems using gradient theory. International Journal of Plasticity 20 (6).
Wilson, 1998. Can design with easy open end. International Application published under the patent cooperation treaty, International Publication Number WO 98/55366.

Zervos, A., Papanastasiou, P., Vardoulakis, I., 2001. Modelling of localisation and scale effect in thick-walled cylinders with gradient elastoplasticity. International Journal of Solids and Structures 38 (30–31), 5081–5095.

Zysset, P.K., Curnier, A., 1996. An implicit projection algorithm for simultaneous flow of plasticity and damage in standard generalized materials. International Journal for Numerical Methods in Engineering 39 (18), 3065–3082.